Supporting Information

Influence of the defect density on the ordering of an NHC monolayer on a silicon surface

Robert Zielinski, Mowpriya Das, Canan Kosbab, Mike Thomas Nehring, Mario Dähne, Norbert Esser, Martin Franz, Frank Glorius

Contents

1 Chemical Synthesis

1.1 General information

The reactions were performed in oven-dried glassware under an atmosphere of dry argon, unless otherwise stated. Air- and moisture-sensitive compounds were stored and handled under an argon atmosphere in a glovebox or by standard Schlenk techniques. All products were dried *in vacuo*. The synthesis of starting materials or synthetic precursors for NHCs (including CO_2-adducts) was not optimized regarding yield.

Dry solvents (acetonitrile, THF, diethyl ether, DMF, hexane, toluene, and DCM) were purified using a custom solvent purification system equipped with activated alumina columns and collected under a positive argon pressure (toluene, n-hexane and DCM over CaH_2; THF and Et_2O over sodium/ketyl benzophenone). The other dry solvents (<50 ppm H_2O) were purchased from Acros Organics, Carl Roth, Fluorochem, Sigma-Aldrich, or VWR and stored over activated molecular sieves under argon. Solvents for extraction, crystallization, and column chromatography were technical grade and purified by atmospheric pressure distillation before use. All reagents were obtained from ABCR, Acros Organics, Alfa Aesar, Carbolution Chemicals, Carl Roth, Chempur, Combi-Blocks, Fisher Scientific, Fluorochem, Merck, Sigma-Aldrich, TCI Europe or VWR and utilized as received, unless otherwise stated.

Analytical thin layer chromatography (TLC) was performed on silica gel 60 F_{254} aluminum plates (Merck). Visualization of the compounds was achieved by UV light (254 nm, 366 nm) or an appropriate staining solution (basic aqueous $KMnO_4$ solution) followed by heating. Flash column chromatography was performed on using silica gel (60 Å, 0.035-0.070 mm, Acros) and an argon pressure of ~0.5 bar. [1]H and ^{13}C spectra were recorded using Brucker 400 MHz spectrometer. The signals are expressed as chemical shifts (δ) in ppm relative to tetramethylsilane with the residual proton signal of the corresponding deuterated solvent as the reference for ^{1}H and ^{13}C NMR spectra (DMSO$-d_6$: δ_H = 2.50 ppm, δ_C = 39.52 ppm) and rounded at the 2nd decimal digit for ^{1}H, 1st for ^{13}C NMR signal. ESI-MS spectra were either recorded on a Bruker MicroTOF or on a Thermo Scientific Orbitrap LTQ XL.

1.2 Synthesis of cyCAAC·CO₂ adduct

2-(2,6-Diisopropylphenyl)-3,3-dimethyl-2-azaspiro[4.5]dec-1-en-2-ium-1-carboxylate (cyCAAC·CO₂): The titled compound was synthesized as shown in Figure S1 by following a literature known procedure.[1] In an oven dried Schlenk tube equipped with stirring bar, LDA (182.1 mg, 1.7 mmol, 1.7 equiv.) and **cyCAAC · HCl** (362 mg, 1.0 mmol, 1.0 equiv.) were taken from the glove box. Then the flask was cooled to -78 °C and dry diethyl ether (7 mL) was added slowly via syringe, dripping on the walls of the flask to cool the solvent. After completion of the addition, the suspension was warmed at room temperature under vigorous stirring for 30 min during which the solution became pale yellow. Then all the volatiles were removed *in vacuo*, and the residue was taken-up under argon with dry hexane (10 mL). The suspension was filtered through a short pad of pre-dried Celite® in a flame-dried frit under argon atmosphere, then the filtrate was collected in a Schlenk tube under argon. Dry CO_2 (dried by bubbling through concentrate sulfuric acid) was bubbled through a needle into the stirred solution for 45 min. During that time a white precipitate formed and the white solid was collected by filtration, washed three times with dry hexane, then dried *in vacuo*, affording the title compound as a white powder (140 mg, 0.379 mmol, 38% yield).

[1]**H NMR** (400 MHz, DMSO$-d_6$) δ 7.51 – 7.43 (m, 1H), 7.40 – 7.31 (m, 2H), 2.77 – 2.64 (m, 2H), 2.38 (s, 2H), 1.97 – 1.82 (m, 4H), 1.80 – 1.61 (m, 3H), 1.41 (s, 8H), 1.30 – 1.15 (m, 13H).

[13]**C NMR** (101 MHz, DMSO$-d_6$): δ (ppm) 192.0, 157.6, 145.5, 130.4, 128.8, 125.4, 79.5, 52.2, 43.6, 35.2, 29.0, 28.5, 26.0, 24.5, 24.2, 21.3.

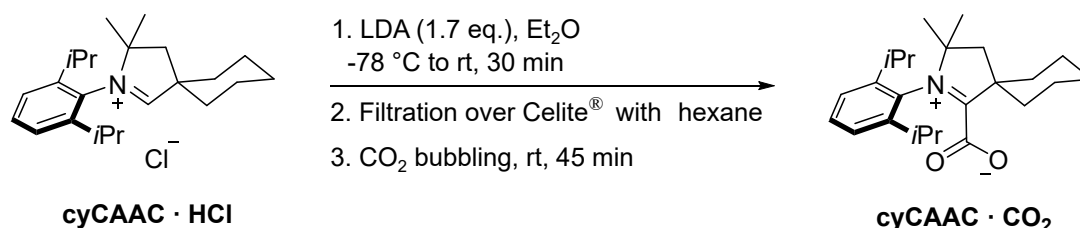**HRMS** (ESI): *m/z* calculated for $C_{24}H_{36}NO_2$ [M+H]$^+$ 370.2746, found 370.2740.

Figure S1 Synthesis of the cyCAAC·CO₂ adduct.
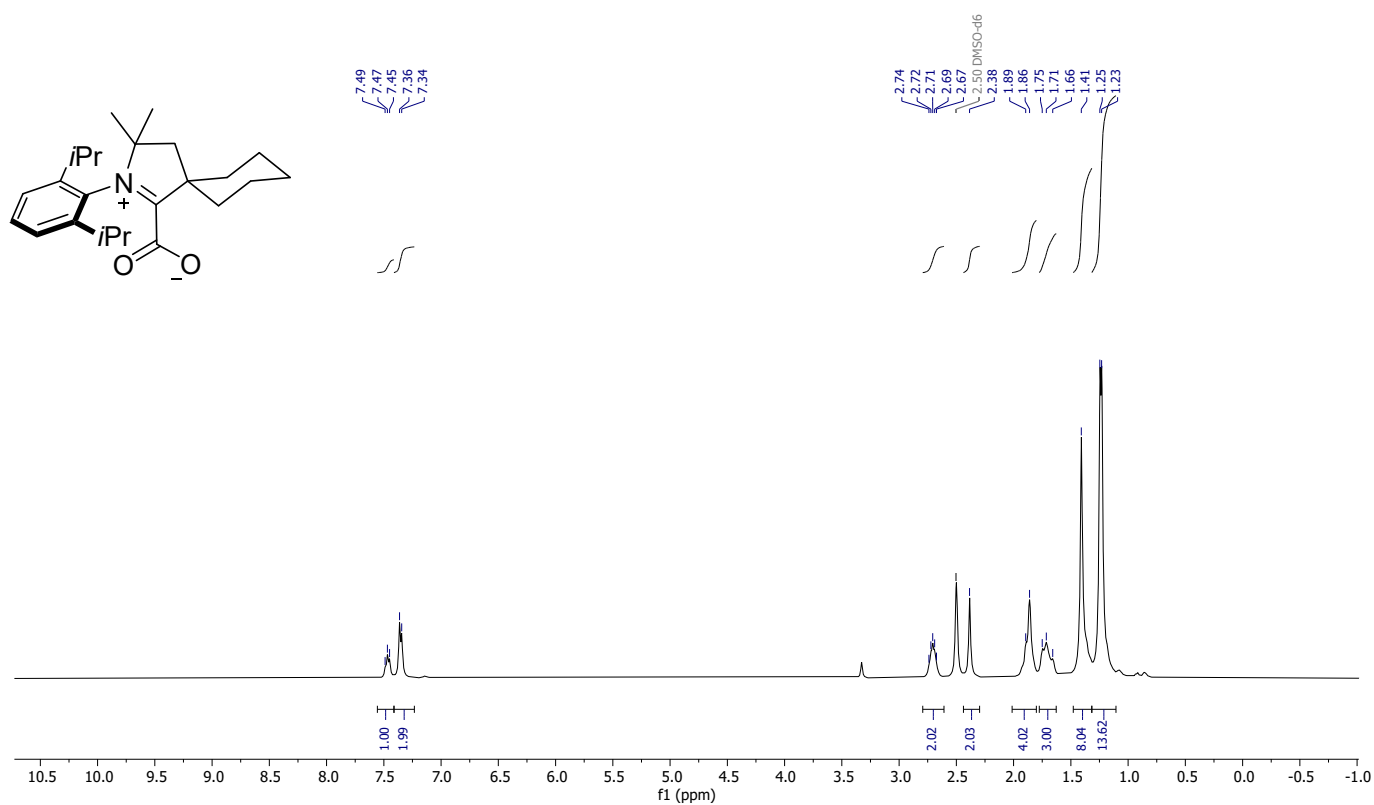
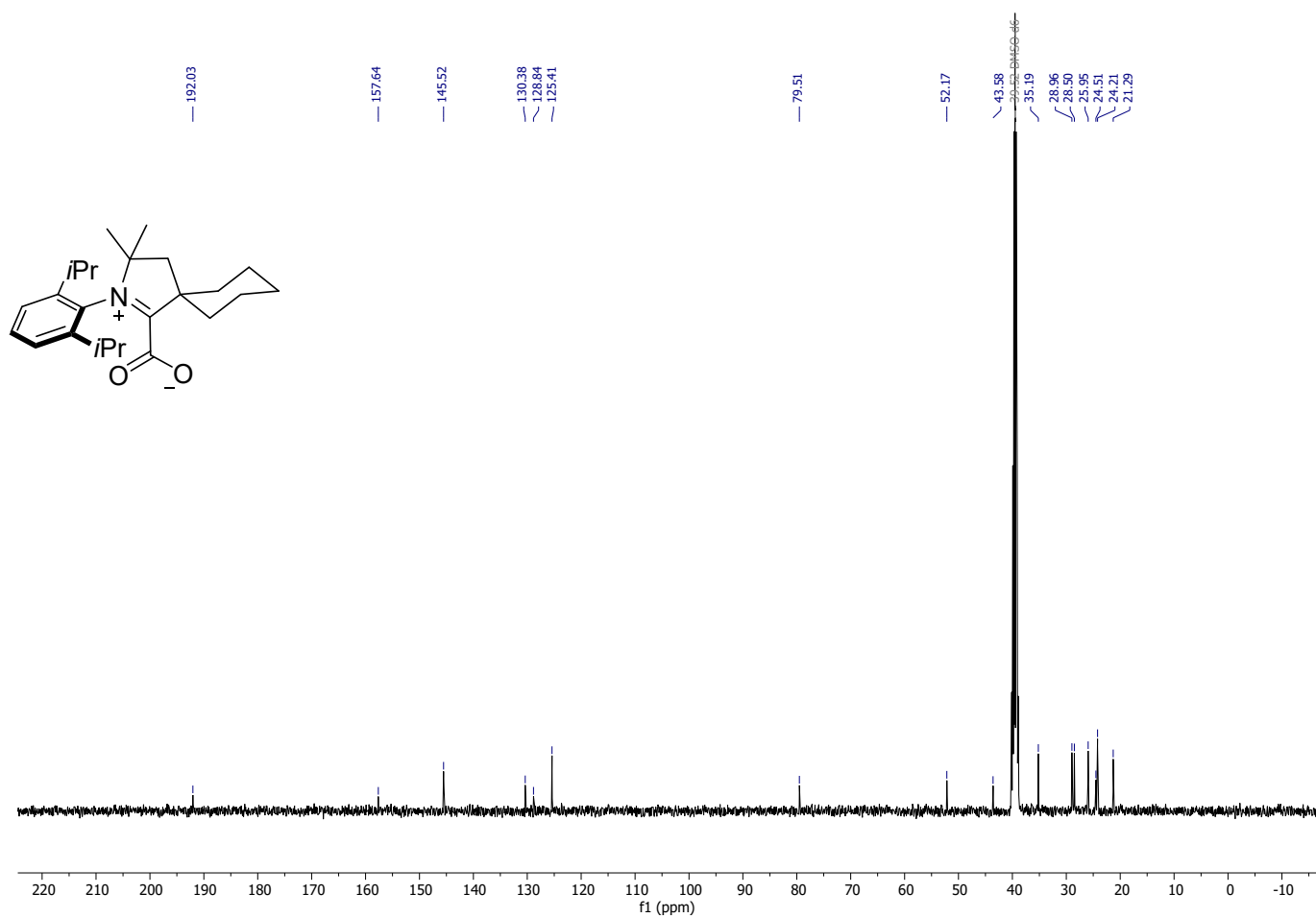**Figure S2** ^{1}H NMR spectra of cyCAAC·CO_2 adduct.

Figure S3 ^{13}C NMR spectra of cyCAAC·CO_2 adduct.

2 Experimental Details

2.1 Sample preparation

After transfer into UHV, all samples were prepared from highly B doped Si(111) wafers by initially degassing the sample at 600 °C for at least 10 hours and subsequent repeated flash annealing up to 1150 °C to remove surface contamination. The samples were heated by a direct current and the temperature was monitored using an infrared pyrometer with an accuracy of ± 20 °C. After the last flash annealing step the sample was heated at 950 °C for 40 min in order to promote the segregation of B dopant atoms to the surface, finally leading to the $(\sqrt{3} \times \sqrt{3})R30°$ reconstruction.

Two wafers with different level of B doping were used for comparison: The resistivity (given by the suppliers) of the higher doped wafer of <0.002 Ωcm correlates with a doping of $>6 \cdot 10^{19}$ cm^{-3}, while the one of the low doped Si(111)-B wafer of <0.005 Ωcm correlates with $>2 \cdot 10^{19}$ cm^{-3}.[2]

The cyCAAC molecules were deposited *in situ* on the sample while held at room temperature, using home–built evaporators with pyrolytic boron nitride crucibles filled with the cyCAAC·CO_2 adducts and a crucible temperature of ~ 35 °C. The deposition was monitored with a quadrupole mass spectrometer using the CO_2 signal at 44 atomic mass units. This resulted in deposition times between a few seconds and several minutes for the investigated low- and high-coverage samples, respectively. During the entire sample preparation process, the pressure did not exceed 2×10^{-7} Pa.

2.2 STM and LEED experiments

The scanning tunneling microscopy (STM) and low energy electron diffraction (LEED) experiments were carried out using a multi-chamber ultra-high vacuum (UHV) system. The base pressure in the STM chamber was 5×10^{-9} Pa and the ones in the preparation chambers were $1\text{-}5 \times 10^{-8}$ Pa. All experiments were done at room temperature. A home-built STM equipped with commercial Nanonis control electronics was used. STM measurements were done using electrochemically etched tungsten tips, which were cleaned *in situ* by electron bombardment. All STM images were aquired using the constant current mode. Furthermore, LEED was used to verify the surface periodicities of the clean substrate and of the cyCAAC monolayer. Therefore, Vacuum Science Instruments ErLeed 150 optics and SPECS 3000D control electronics were used.

2.3 XPS measurements

X-ray photoemission spectroscopy (XPS) was used to determine the work function change as well as to investigate the sample composition. The measurements were performed *in situ* in a separate UHV system providing equivalent sample preparation options (base pressure of 3×10^{-8} Pa), using a hemispherical energy analyser (SPECS Phoibos 100) and monochromatized Al$_{k\alpha}$ X-rays with hν = 1,486.7 eV (SPECS FOCUS 500 ellipsoidal crystal monochromator and X-ray source SPECS XR50 M), yielding an instrumental resolution of ~ 0.5 eV. The work function change upon formation of the cyCAAC monolayer was determined by measuring the secondary electron onsets for the clean substrate as well as for the cyCAAC monolayer as described e.g. in Ref. 3. To ensure that all secondary electrons reached the analyser, a negative potential of 9 V was applied to the sample.

3 The Si(111)$(\sqrt{3} \times \sqrt{3})$R30° surface

The exact structure of the Si(111)$(\sqrt{3} \times \sqrt{3})$R30° (Si(111)-B) surface was identified in 1989 by Headrick et al.[4] using synchrotron X-ray diffraction. In parallel, Bedrossian et al.[5] and Lyo et al.[6] also identified the structure using a combination of scanning tunneling microscopy and spectroscopy as well as first-principles calculations. This structure is widely accepted, later it was also confirmed and refined by dynamical low-energy electron diffraction and photoelectron diffraction.[7,8] The corresponding structural model is shown in Figure S4(a,b). The topmost layer of the reconstruction is formed by Si adatoms, residing in the so-called T_4 position, while the B atoms substitute Si atoms in the second layer on so-called S_5 sites (a good description of the different adsorption sites can be found in Ref. 9). This leads to an electron transfer from the dangling-bonds at the Si adatoms to the B atoms and in the end to a passivated surface.

However, occasionally also point defects form. The structure models of the most important ones are depicted in Figure S4(c). In the so-called Si-Si(S_5) defect, the Si atom underneath the adatom is not substituted by B leading to a non-passivated adatom. As the probability to substitute all Si atoms on S_5 sites depends on the B concentration in the bulk, the density of Si-Si(S_5) defects can be influenced by the doping concentration as demonstrated in Section 4. Other common defects are adatom vacancies, where no Si adatom formed on the T_4 site. For such vacancies, two different types exist. In the V-B(S_5) case, the S_5 site is occupied by a B atom and in the V-Si(S_5) case by a Si atom.
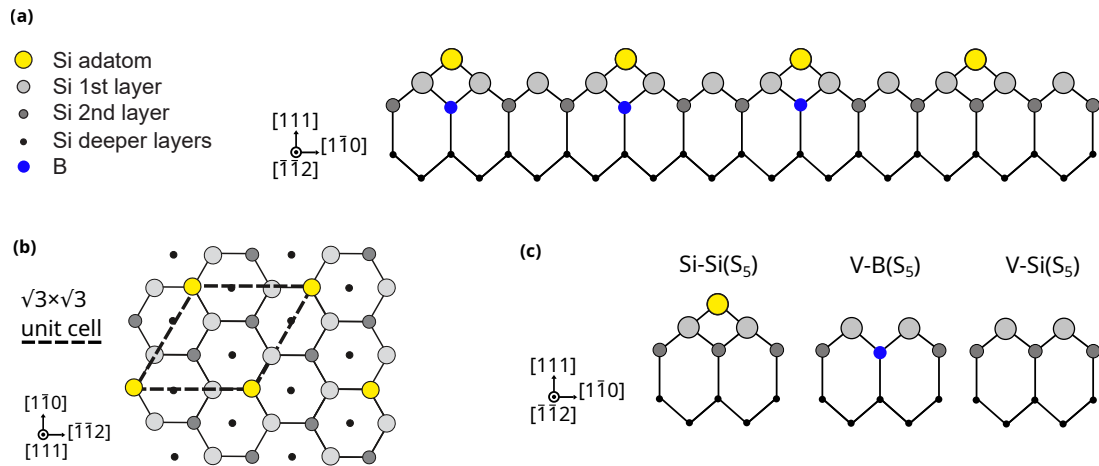

Figure S4 Structure model of the ideal Si(111)-B surface in (a) sideview and (b) topview. The typical defects are presented in (c).

4 Determination of the defect densities

The defect density is determined by counting the individual defects of the clean surface for both used wafers in large-scale STM images. In Figure S5 examples of such images are shown. In the STM image of the higher doped wafer shown in (a), the characteristic point defects described in the previous section are indicated. From an analysis of several STM images, the defect densities for the different defect types are determined. The results are summarized in Table S1. As can be seen already at first sight by visually comparing the STM images in (a) and (b), the defect density for the lower doped wafer is much higher. As an indication of all defects would make the figure confusing, only examples of the defects are indicated. Instead, a detail of the image with all defects indicated is shown as an inset. Due to the high defect density in (b), the rather small differences between the V-Si(S_5) and V-B(S_5) defects are not visible any more, thus their densities are merged in Table S1.

Although the density of the vacancy defects also slightly increases, the main increase in the defect density is found for the Si-Si(S_5) defects (see Table S1). This is also expected as the lower B concentration in the bulk crystal for the lower doped wafer should lead to a lower B concentration at the surface and thus to a higher density of sites where the Si atom at the S_5 site is not substituted with B.
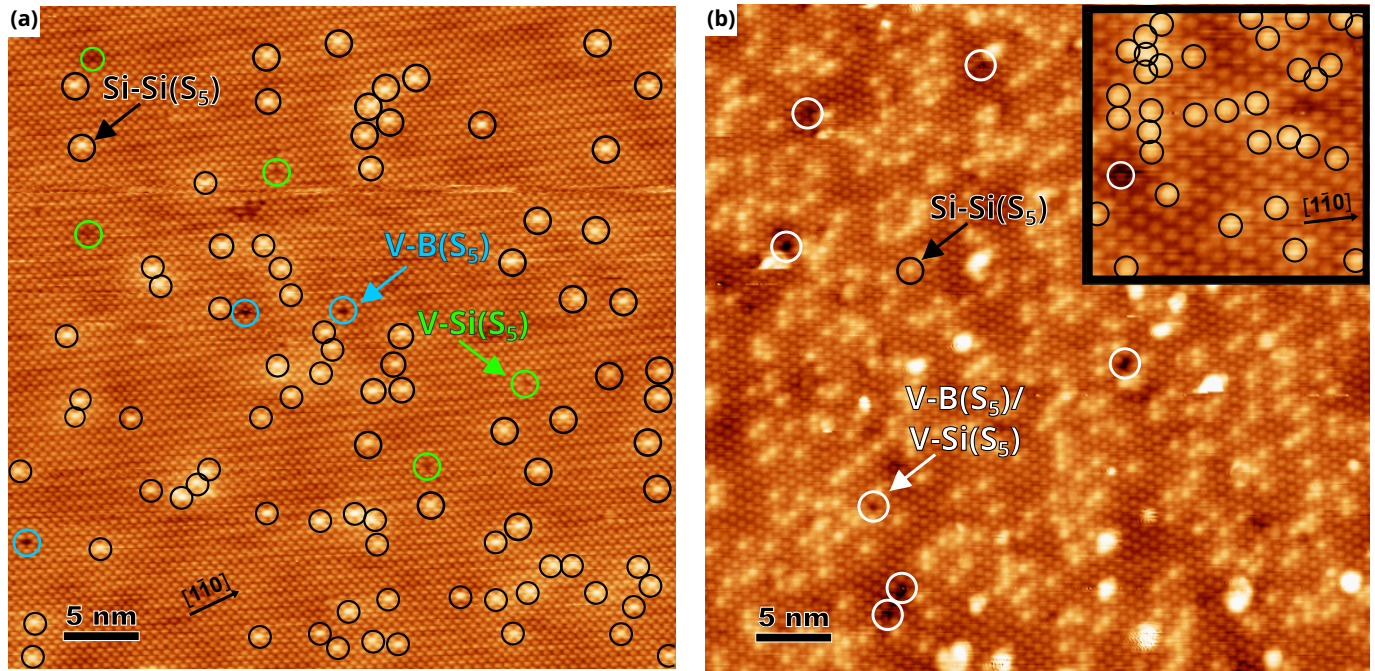

Figure S5 STM images of the clean surfaces of (a) the higher doped wafer ($V_S = +2.0$ V, $I_T = 10$ pA) and (b) the lower doped wafer ($V_S = +1.8$ V, $I_T = 50$ pA) with a more detailed inset. Marked are the typical defects.

Table S1 Properties of the two different Si(111) wafers used in this work.

	Higher doped Wafer	Lower doped Wafer
Resistivity (Ωcm)	<0.002	<0.005
Dopant concentration (10^{-19} cm^{-3})	>6	>2
Si-Si(S_5) defect density (10^{12} cm^{-2})	3.13	25.05
Sum of V-B(S_5) and V-Si(S_5) defect densities (10^{12} cm^{-2})	0.68	0.99
Overall defect density (10^{12} cm^{-2})	3.81	26.04

5 Determination of the cyCAAC monolayer domain sizes

In Figure S6, STM images of the cyCAAC monolayers formed on (a) the higher doped wafer and (b) the lower doped wafer are presented. In (a), large 3×3 ordered domains form, separated by domain boundaries. The reason for the formation of different domains is the larger periodicity of the 3×3 overlayer with respect to the $\sqrt{3} \times \sqrt{3}$ substrate and the resulting existence of three different sublattices. An initial adsorption on a different sublattice then leads to the formation of a domain boundary when the growing domains touch each other.

By comparing the STM images in (a) and (b), it is obvious that the average domain size is much larger for the higher doped wafer. Thus, the domain size has to coincide with the defect density and the initial adsorption is assumed to take place on a defect. To quantitatively underpin this observation, the domain sizes on the two different wafers are determined by marking the domain boundaries and counting the number of domains per area. In (a), this is easily possible as shown in the image. However, the domains on the lower doped wafer are often formed by only a few cyCAAC molecules as the defect density is very high. Thus, the analysis is again only shown for an example region in the inset. As for the defect density, the analysis of the domain size was again done for several large-scale STM images and values of $\sim$130 nm^2 and 10–20 nm^2 are found for the higher and lower doped wafer, respectively.
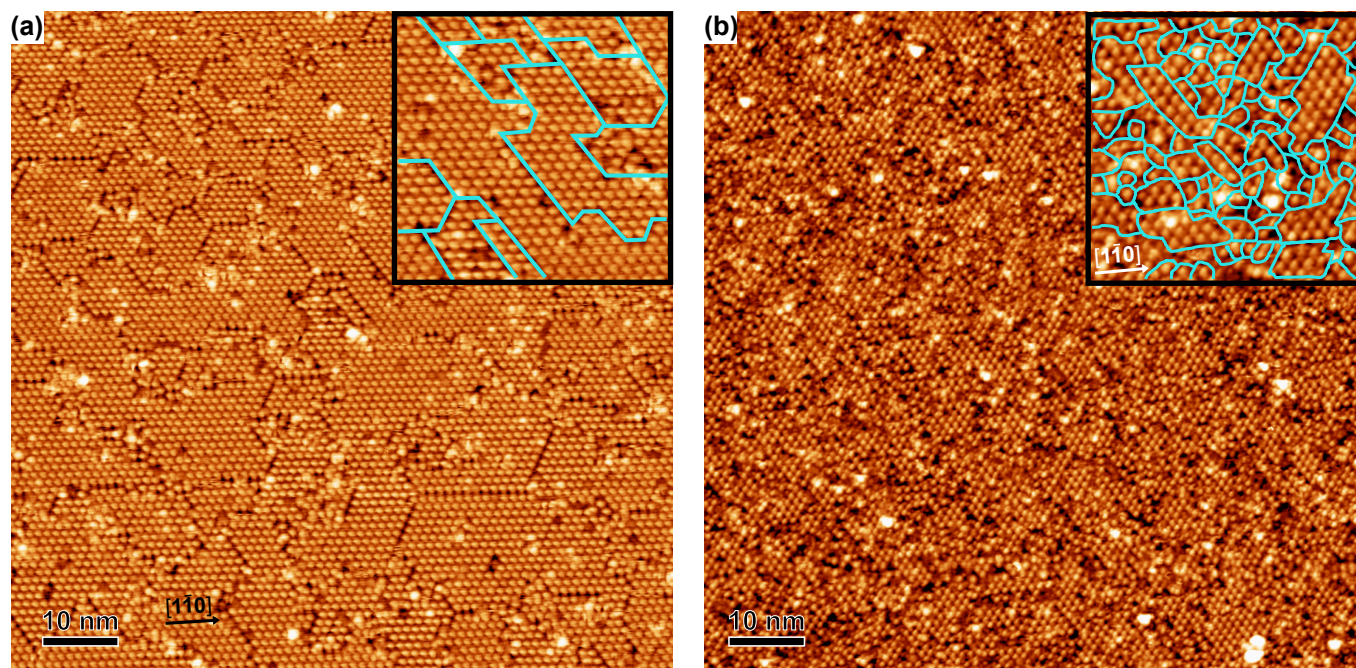

Figure S6 STM images after a full cyCAAC monolayer coverage on (a) the higher doped wafer ($V_S = -2.3$ V, $I_T = 15$ pA) and (b) the lower doped wafer ($V_S = -2.3$ V, $I_T = 15$ pA) with marked domains in the inset.

6 Step height at monolayer cyCAAC coverage

The STM image shown in Figure S7(a) shows an area of the cyCAAC monolayer with a surface step. In (b), a height profile across the step taken along the green line in (a) is shown. The step height is determined to 0.31 nm, corresponding to the monoatomic step height on the Si(111) surface. Also in other STM images of the cyCAAC monolayer with steps only heights corresponding to multitudes of the monoatomic step height are observed. This observation strongly suggests that the room-temperature cyCAAC adsorption saturates at monolayer coverage and no further layers grow, since in the latter case larger step heights are expected. Furthermore, no formation of additional molecular islands is observed on top of the monolayer, further supporting the assumption of a saturation.
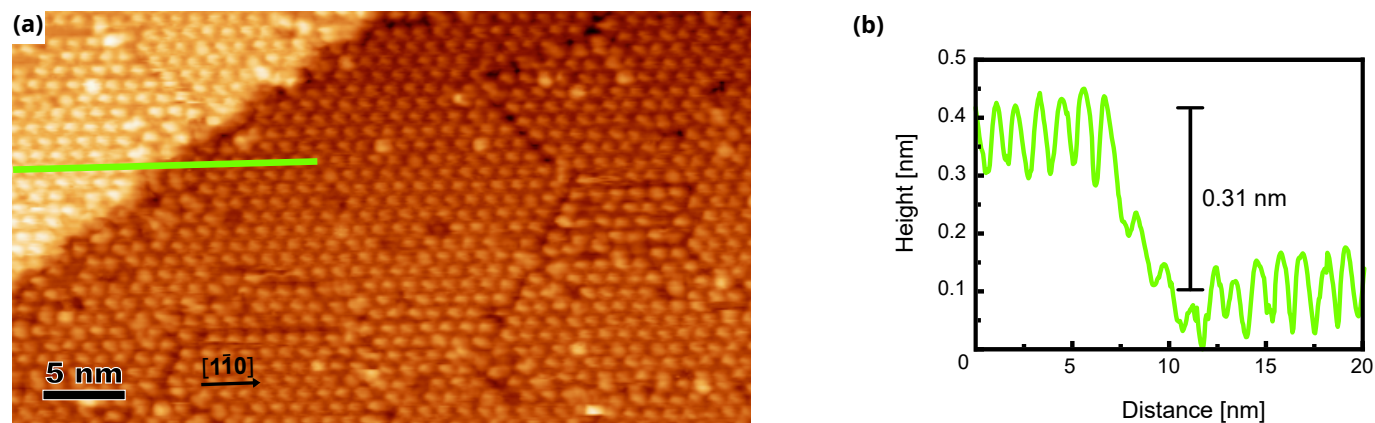

Figure S7 (a) STM image of a full cyCAAC monolyer coverage on the higher doped wafer ($V_S = -2.5$ V, $I_T = 15$ pA) with (b) a height profile taken along the green line in (a).

7 XPS overview spectra

To demonstrate that the Si(111)-B samples investigated here are clean and free of oxides, XPS overview spectra are shown in Fig. S8. For both wafers, the clean Si(111)-B samples show only peaks expected for Si(111)-B, i.e. the Si $2p$ and Si $2s$ core levels and the B $1s$ core level. The latter is visible as a faint peak on top of a plasmon loss satellite of the Si $2s$ core level (indicated by arrows in (a), see also Ref. 10).

For the cyCAAC monolayers, only additional peaks related to the molecules (C $1s$ and the N $1s$) appear. This further demonstrates a clean cyCAAC deposition without residuals from the detached CO_2 molecules. The larger C $1s$ signal in (b) is related to the different measurement geometry, while the molecular density is slightly lower than in (a) because of the influence of the domain boundaries.

In the region of the O $1s$ signal around 530 eV, no signal is detected for all samples.
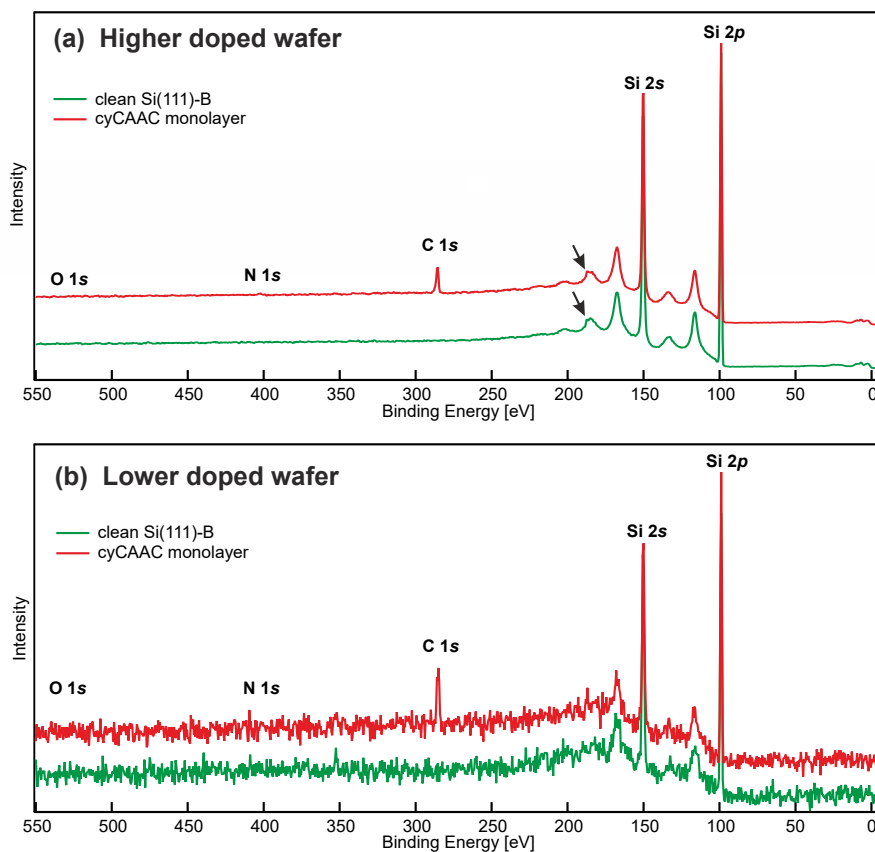

Figure S8 XPS overview spectra for the clean Si(111)-B samples and cyCAAC monolayers on (a) the higher doped wafer (measured in normal emission) and (b) the lower doped wafer (measured under an emission angle of 60°).

References

[1] J. Ren, M. Freitag, Y. Gao, P. Bellotti, M. Das, B. Schulze Lammers, H. Mönig, Y. Zhang, C. G. Daniliuc, S. Du, H. Fuchs and F. Glorius, *Angew. Chem. Int. Ed.*, 2022, **61**, e202115104.

[2] S. M. Sze and K. K. Ng, *Physics of Semiconductor Devices*, Wiley, 3rd edn, 2006.

[3] H. Lüth, *Solid Surfaces, Interfaces and Thin Films*, Springer, Cham, 6th edn, 2014.

[4] R. L. Headrick, I. K. Robinson, E. Vlieg and L. C. Feldman, *Phys. Rev. Lett.*, 1989, **63**, 1253–1256.

[5] P. Bedrossian, R. D. Meade, K. Mortensen, D. M. Chen, J. A. Golovchenko and D. Vanderbilt, *Phys. Rev. Lett.*, 1989, **63**, 1257–1260.

[6] I.-W. Lyo, E. Kaxiras and P. Avouris, *Phys. Rev. Lett.*, 1989, **63**, 1261–1264.

[7] H. Huang, S. Y. Tong, J. Quinn and F. Jona, *Phys. Rev. B*, 1990, **41**, 3276–3279.

[8] P. Baumgärtel, J. J. Paggel, M. Hasselblatt, K. Horn, V. Fernandez, O. Schaff, J. H. Weaver, A. M. Bradshaw, D. P. Woodruff, E. Rotenberg and J. Denlinger, *Phys. Rev. B*, 1999, **59**, 13014–13019.

[9] F. Bechstedt, *Principles of Surface Physics*, Springer, Berlin, Heidelberg, 2003.

[10] M. Franz, S. Chandola, M. Koy, R. Zielinski, H. Aldahhak, M. Das, M. Freitag, U. Gerstmann, D. Liebig, A. K. Hoffmann, M. Rosin, W. G. Schmidt, C. Hogan, F. Glorius, N. Esser and M. Dähne, *Nat. Chem.*, 2021, **13**, 828.